

<https://doi.org/10.1038/s43247-024-01668-1>

The Yangtze River Delta experienced strong seasonality and regular summer upwelling during the warm mid-Holocene



Matthias Alberti^{1,2}✉, Sandro F. Veiga^{3,4}, Bo Chen⁵, Liang Hu⁶, Zheng Fang¹, Baochun Zhou⁷ & Yanhong Pan¹✉

The mid-Holocene climate optimum saw warm temperatures in large parts of China, but its impact on seasonal environmental changes is not fully understood yet. Here, we use high-resolution geochemical analyses of 7000 to 6000 year-old oyster shells from the Yangtze River Delta to reconstruct climatic and oceanographic patterns. The stable isotope ($\delta^{18}\text{O}$, $\delta^{13}\text{C}$) and clumped isotope data reflect prominent seasonal changes in temperature, precipitation, and river discharge. Summer months experienced warm temperatures and a distinct increase in rainfalls and river discharge. In contrast, winter months were characterized by a dry season, which might have been longer than today. Stable isotope data also indicate regular summer upwelling in the study area. These results partly disagree with available climate models raising doubts on the models' reliability. Thus, our palaeo-proxy data offers the possibility to evaluate and correct climate models and thereby improve predictions for the future considering on-going global warming.

During the mid-Holocene, most parts of China experienced a phase of warm temperatures, the so-called mid-Holocene climate optimum, which lasted from about 8000 to 6000 years BP depending on the exact locality^{1–4}. In the Yangtze River Delta of eastern China (Fig. 1), the mid-Holocene saw prominent steps in the development of human civilization including the spread of settlements across the growing delta plain, the introduction of rice cultivation, and the formation of larger towns^{5–8}. The fates of these early humans were strongly influenced by environmental changes, but humans generally prospered on the delta plain in the following millennia, which were characterized by a gradual cooling of up to 2 °C in average temperatures until pre-industrial times^{4,9}. Today, the Yangtze River Delta is a densely populated region with enormous economic importance and a population of more than 100 million people in the delta region itself¹⁰. Following the latest IPCC report, global average temperatures are rising by 3 °C or more (compared to pre-industrial times) until the end of the 21st century, if humans are not able to drastically lower emissions of greenhouse gases¹¹. The warm mid-Holocene provides a suitable scenario for East China to

observe effects of a warmer climate on environmental parameters such as precipitation and monsoon strength.

The present study uses high-resolution geochemical analyses of fossil oyster shells from the Yangtze River Delta to reconstruct seasonal climate and oceanographic patterns in the mid-Holocene, which were unknown for the region so far. These proxy data are then compared with the results of climate models for the mid-Holocene, the conditions of today, and simulations for the future considering ongoing global warming. In combination, the study provides a better understanding of mid-Holocene environments as well as offers predictions for future environmental changes in the delta region.

Presently, the Yangtze River Delta is characterized by a humid subtropical climate with an annual temperature average of 15–16 °C (see Supplementary Information 1; Fig. S1). Winters are cold and dry with little precipitation. Summers are hot and humid with stronger rainfalls, particularly during the monsoon months (June–August). The discharge of the Yangtze River also follows a well-documented seasonal pattern with much

¹State Key Laboratory for Mineral Deposits Research, School of Earth Sciences and Engineering, Centre for Research and Education on Biological Evolution and Environment and Frontiers Science Center for Critical Earth Material Cycling, Nanjing University, Nanjing, China. ²Geologisches und Mineralogisches Museum, Institut für Geowissenschaften, Christian-Albrechts-Universität zu Kiel, Ludwig-Meyn-Str. 12, Kiel, Germany. ³School of Atmospheric Sciences and Key Laboratory of Mesoscale Severe Weather/Ministry of Education and Frontiers Science Center for Critical Earth Material Cycling, Nanjing University, Nanjing, China. ⁴Nanjing-Helsinki Institute in Atmospheric and Earth System Sciences, Nanjing University, Suzhou, China. ⁵State Key Laboratory of Palaeobiology and Stratigraphy and Center for Excellence in Life and Palaeoenvironment, Nanjing Institute of Geology and Palaeontology, Chinese Academy of Sciences, Nanjing, China. ⁶Institute of Sedimentary Geology, Chengdu University of Technology, Chengdu, China. ⁷Shanghai Natural History Museum, Shanghai, China.

✉e-mail: matthias.alberti@ifg.uni-kiel.de; panyanhong@nju.edu.cn

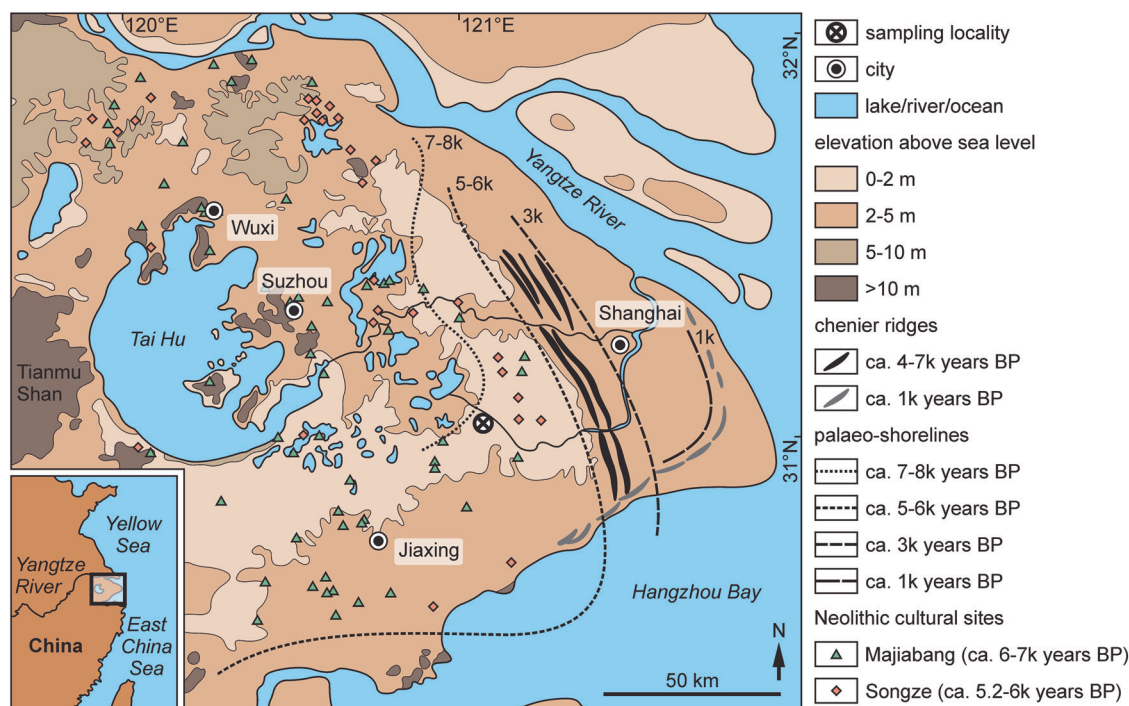


Fig. 1 | Map of the study area in the southern Yangtze River Delta. The sampling site of the analyzed mid-Holocene oyster shells is situated ca. 40 km southwest of Shanghai. The palaeo-shorelines, chenier ridges, and Neolithic cultural sites illustrate the delta progradation during the Holocene^{6,8,87–89}.

higher water levels in the summer months compared to the dry winter. Oceanographic conditions in the adjacent East China Sea have been studied intensely in the last decades^{12–17}, but detailed observations over long, centennial time intervals are lacking. In general, the salinity of coastal surface waters is determined by the seasonal strength in river discharge^{17–21}. In addition, the interplay of the Taiwan Warm Current, the China Coastal Current (also called Zhejiang-Fujian Coastal Current), and the Kuroshio Current together with its branches contribute to the mixing of water masses and the influx of saline waters in the delta region¹⁶. Further research in recent years concentrated on the causal relationships and seasonal occurrences of alongshore winds, coastal upwelling, phytoplankton blooms, and hypoxia^{22–29}, but observations spanning long-time intervals are still missing. It is at this point, that comparisons between present-day observations with seasonal reconstructions from the Holocene can add particularly valuable information.

Results

Three shells of the oyster *Crassostrea gigas* were selected from an oyster reef in the central delta plain, approximately 40 km southwest of Shanghai (Fig. 1). Radiometric dating resulted in conventional radiocarbon ages of 7030, 6550, and 6160 ± 30 years BP for shells 1 to 3 (Supplementary Information 1). The fossils (Fig. 2) were cut through the hinge along the major growth axis. Thin-sections covering the hinge region were produced and examined with petrographic and cathodoluminescence microscopes. Samples were taken with a computer-controlled micromill for stable isotope analysis and with a hand-held dental drill for clumped isotope analysis.

Macroscopic and microscopic observations

Macroscopic and microscopic observations (Fig. 2; compare Supplementary Information 1; Figs. S2–S6) show that the hinge is the most compact part of each shell. Growth increments are visible in most sections and comparatively wide in shells 1 and 2 and narrower in shell 3. The internal surfaces of the hinges are wrinkled, particularly in the older parts of the shells. Similar to earlier observations³⁰, concave depressions on the hinge surface correspond to winter seasons, while convex ridges formed during summer months. However, this pattern is less clear in shell 3 and also seems to be lost in the

younger parts of shell 1. Colour changes within growth bands also seem to reflect changing seasonal growth rates (e.g., via crowding of growth layers during winter months). Spawning shocks are not visible in the thin-sections or only cause faint, inconspicuous growth lines (compare Fig. 2G–I).

When examined with a cathodoluminescence microscope, the calcite of the hinge appears largely dark and non-luminescent (Fig. S5). Weak and cloudy orange luminescence can be seen along some of the growth layers. In contrast, strong luminescence characterizes the chalky parts of the shell. Following previous research, a predominantly non-luminescent, calcitic shell indicates no diagenetic alteration^{30–33}. The comparatively weak luminescence seen along some growth layers is similar to previously published observations on recent shells of *C. gigas*³⁴, which did not experience any diagenetic alteration^{35,36}.

Following macroscopic and microscopic observations, the hinge areas of shells 1 to 3 were selected as targets for high-resolution stable isotope analysis (Fig. 2J–L; for a more detailed description of the fossils see Supplementary Information 1).

Stable isotope analyses

Results of the high-resolution stable isotope analyses of all three sampled shells show a prominent cyclic pattern in both $\delta^{18}\text{O}$ and $\delta^{13}\text{C}$ values (Fig. 3A, B; Fig. S7; Supplementary Data 1). Maxima in $\delta^{18}\text{O}$ values (reflecting cold winter conditions) are relatively sharp, while minima (corresponding to summer months) are broader. The same pattern is also visible in $\delta^{13}\text{C}$ values, which show a strong positive correlation to $\delta^{18}\text{O}$ values (Fig. S8). However, the decrease in $\delta^{13}\text{C}$ values at the beginning of each cycle is commonly delayed compared to the $\delta^{18}\text{O}$ values (seen particularly well in cycles 3 to 8 of shell 1 or in cycle 3 of shell 2). Furthermore, almost all cycles show second-order excursions of $\delta^{18}\text{O}$ and $\delta^{13}\text{C}$ values towards more positive values situated within the broad minima.

The minima and maxima for measured stable isotope values are largely comparable throughout the lifetime of each individual. The amplitude of the signal decreases somewhat in cycles with a lower sampling resolution, which is most likely a sampling artifact and not an original signal. This is particularly a problem for shell 3, which has only one cycle with a higher sampling resolution (cycle 2). Shell 1 shows a decrease in the width of the cycles

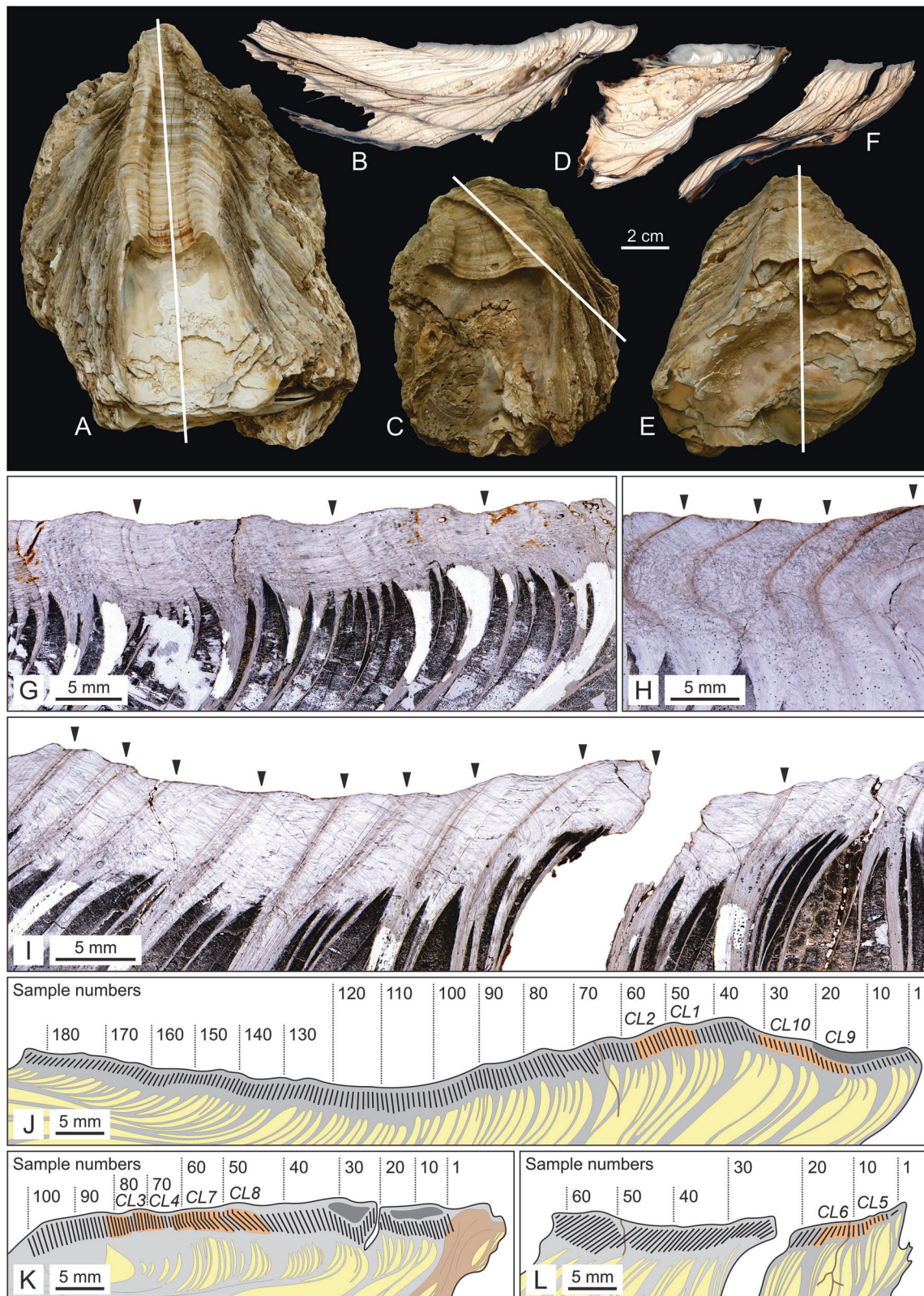


Fig. 2 | Documentation of the three analyzed mid-Holocene oysters from the Yangtze River Delta. Interior views and sampled longitudinal sections of the three analyzed mid-Holocene shells of the oyster *Crassostrea gigas* from the Yangtze River Delta (lines indicate position of sections; A, B: Shell 1; C, D: Shell 2; E, F: Shell 3). Thin-sections through the hinges show darker bands reflecting growth increments

(arrows indicate the position of winter growth breaks; G, H: Shell 1; I: Shell 3). Sketches of the hinge area of the three shells show the position of samples used for high-resolution stable isotope analysis (simple numbers) and clumped isotope analysis (CL1 to CL10). Dark-grey and brown areas inside the shells indicate discolorations avoided during sampling (J: Shell 1; K: Shell 2; L: Shell 3).

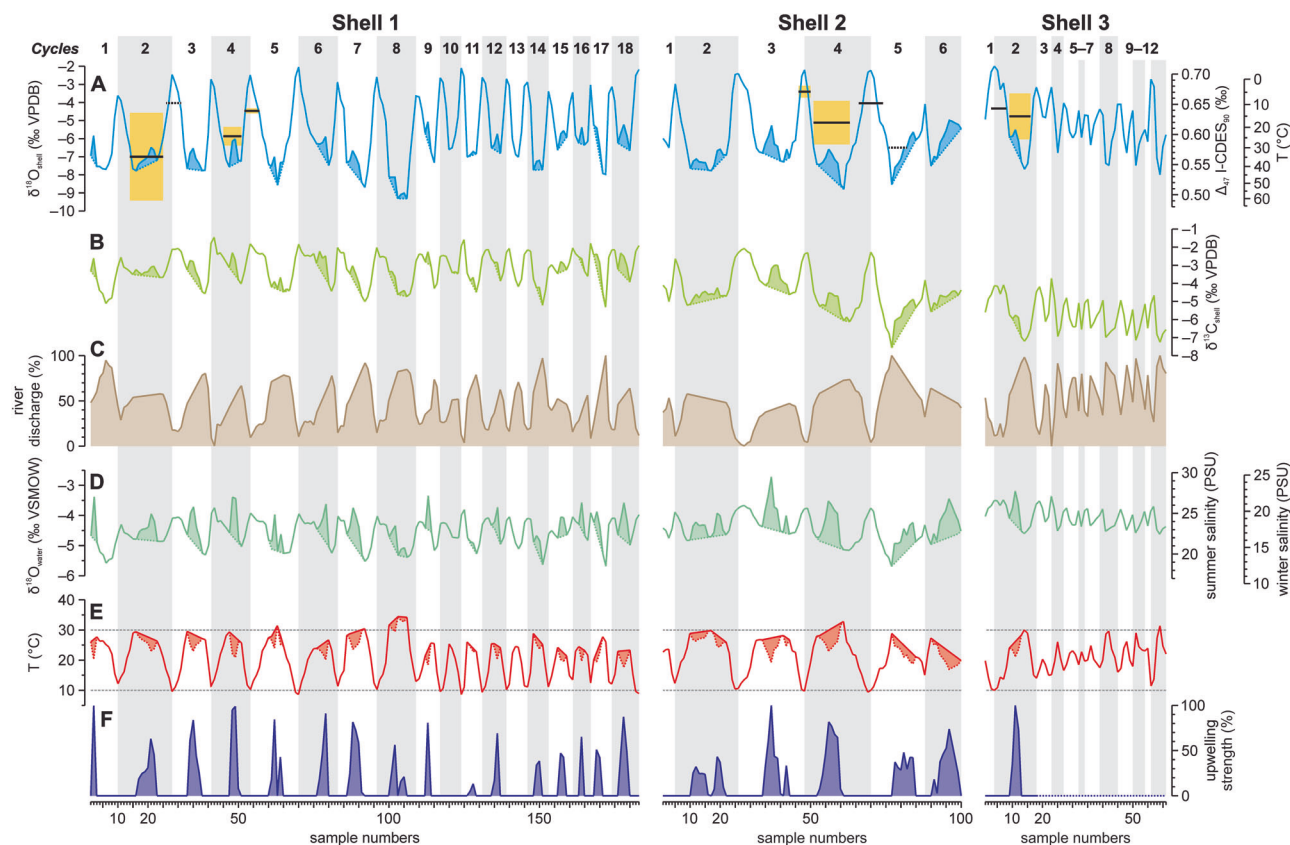


Fig. 3 | Results and interpretations of the geochemical analyses of the three mid-Holocene oysters from the Yangtze River Delta (see Supplementary Information 1 for details). A, B The $\delta^{18}\text{O}_{\text{shell}}$ and $\delta^{13}\text{C}_{\text{shell}}$ values show prominent first-order cycles with sharp maxima and broad minima. Furthermore, second-order excursions towards more positive values can be found within the broad minima (shaded). Results of clumped isotope analyses (in black and yellow) often show high standard deviations. The temperature scale for the Δ_{47} values is calculated based on Meinicke et al.^{46,47}. Yellow shading represents ± 1 standard deviation. Dotted lines for samples CL3 (summer season of cycle 5 in shell 2) and CL10 (winter season between cycles 2 and 3 in shell 1) indicate samples with only one measurement (compare

Supplementary Data 2). C Relative river discharge strength estimated based on first-order cycles in $\delta^{13}\text{C}_{\text{shell}}$ values (B). D Seasonal changes in $\delta^{18}\text{O}_{\text{water}}$ values estimated for reconstructed river discharge (C) and a proposed general temperature seasonality of 10 to 30 °C. Variations in $\delta^{18}\text{O}_{\text{water}}$ values can also be connected to seasonal salinity fluctuations⁴¹. Shaded areas of the curves indicate the impact of the second-order excursions in $\delta^{18}\text{O}_{\text{shell}}$ values. E Seasonal water temperatures were calculated based on measured $\delta^{18}\text{O}_{\text{shell}}$ values (A) and estimated $\delta^{18}\text{O}_{\text{water}}$ values (D). Shaded areas of the curves indicate the impact of the second-order excursions in $\delta^{18}\text{O}_{\text{shell}}$ values. F Upwelling strength estimated based on second-order $\delta^{18}\text{O}_{\text{shell}}$ excursions (A).

parallel to the growth direction, especially after cycle 8 (compare Supplementary Information 1)³⁷.

Absolute $\delta^{18}\text{O}$ values are largely comparable between all three specimens, but $\delta^{13}\text{C}$ values are on average higher in shell 1, intermediate in shell 2, and more negative in shell 3 (Fig. 3B; Fig. S8).

Clumped isotope analyses

Following the high-resolution stable isotope analysis, areas of the shells representing summer and winter seasons were resampled for clumped isotope analysis (Supplementary Data 2). Because this method requires much larger sample sizes, the ten collected samples have a lower temporal resolution. Results for Δ_{47} values fluctuate between 0.563 and 0.671 ‰ (I-CDES90), but partly have large analytical uncertainty (Fig. 3A; Table S2; Fig. S9). Large standard deviations are caused by a comparatively low number of repetitions of analyses of single samples. In general, samples were analyzed two or three times, but two samples could be analyzed only once and therefore no standard deviation can be given (see Supplementary Information 1 and Supplementary Data 2). The standard deviations for the clumped isotope analyses are always higher for samples representing summer seasons than those of winter samples. This might indicate a higher heterogeneity in these samples. The clumped isotope samples representing summer seasons show lower values (average: 0.598 ‰) compared to those of winter seasons with higher values (average: 0.651 ‰).

Discussion

Mid-Holocene seasonal environmental patterns

The stable isotope data of the three analyzed oysters reflect prominent seasonal changes (compare Supplementary Information 1 for further discussion; Figs. S10–S13). In general, $\delta^{18}\text{O}$ values of mollusk shells ($\delta^{18}\text{O}_{\text{shell}}$) are negatively correlated with water temperatures and positively correlated with $\delta^{18}\text{O}$ values of the surrounding water body ($\delta^{18}\text{O}_{\text{water}}$)^{38–40}. Because $\delta^{18}\text{O}_{\text{water}}$ values in river water are much more negative than in ocean water, the measured very low $\delta^{18}\text{O}_{\text{shell}}$ values clearly suggest a brackish setting for the study area in the mid-Holocene⁴¹. Because $\delta^{18}\text{O}_{\text{shell}}$ values depend on temperature and $\delta^{18}\text{O}_{\text{water}}$ values, it is not possible to reconstruct both environmental parameters independently. This is particularly difficult in an estuarine setting, where $\delta^{18}\text{O}_{\text{water}}$ values are known to fluctuate considerably. In such a situation, seasonal temperature extremes might be proposed with a higher certainty than changes in $\delta^{18}\text{O}_{\text{water}}$ values. In the following, the different factors influencing the recorded geochemical dataset are discussed in detail.

Previous studies showed that *C. gigas* stops or strongly slows shell growth in cold water during winter months (below ca. 10–12 °C)^{30,42–45}. This explains the sharp $\delta^{18}\text{O}_{\text{shell}}$ maxima observed in the record. Samples collected at these maxima and used for clumped isotope analysis result in average water temperatures of ca. 10 °C (calculated with the equation of Meinicke et al.^{46,47}). On the other end of the spectrum, the maximal

temperatures tolerated by *C. gigas* are about 35 °C, but elevated mortality rates have been noted already at temperatures above 30 °C^{48,49}. Present-day average summer water temperatures in the East China Sea adjacent to the Yangtze River Delta fluctuate between 27 and 28 °C. Considering that the summer months might have been slightly warmer in the mid-Holocene compared to today⁴, the analyzed oysters might have experienced conditions up to around 30 °C. This is close to their upper tolerance limit, but the recorded broad $\delta^{18}\text{O}_{\text{shell}}$ minima indicate that they did not suffer prominent summer growth breaks. Summer temperatures reconstructed based on clumped isotope analyses fluctuate around an average of 24 °C, but due to a stronger averaging over several months this value might not represent peak temperatures during summer months (see also below). Based on observed growth patterns in *C. gigas*, reported present-day and mid-Holocene temperature conditions, and the rough temperature data from clumped isotope analyses, it seems realistic to assume that the measured $\delta^{18}\text{O}_{\text{shell}}$ values reflect seasonal temperature changes somewhere between 10 to 30 °C. Considering measured amplitudes in $\delta^{18}\text{O}_{\text{shell}}$ cycles up to 6–7‰ (Figs. 3A, S7), it becomes evident that the study area must have experienced additional changes in $\delta^{18}\text{O}_{\text{water}}$ values (Figs. S15, S16). This can be explained by seasonal changes in the discharge strength of the Yangtze River, which are also observed today (Fig. S1C, D).

A number of factors can influence $\delta^{13}\text{C}_{\text{shell}}$ values (Fig. 3B) in fossil shells, including taxonomic differences, ontogenetic trends, metabolic changes, variations in primary productivity, upwelling, sea-level changes, ocean currents, or even water temperatures^{43,50–52}. In the present study, the measured $\delta^{13}\text{C}_{\text{shell}}$ values show a prominent seasonal signal with a strong amplitude, thereby excluding most of the mentioned processes. Because river water transports dissolved inorganic carbon, which is generally isotopically lighter compared to oceanic dissolved inorganic carbon⁵³, it seems reasonable to explain the recorded first-order $\delta^{13}\text{C}_{\text{shell}}$ cycles by seasonal changes in fluvial influx as observed today⁵⁴. It is therefore plausible to use the first-order $\delta^{13}\text{C}_{\text{shell}}$ cycles as a proxy for river discharge strength (Fig. 3C; Fig. S18)⁵⁴. Furthermore, the amount of river influx directly determines the $\delta^{18}\text{O}_{\text{water}}$ value.

Combining the assumed seasonal temperature minima and maxima recorded by *C. gigas* with $\delta^{13}\text{C}_{\text{shell}}$ values as a proxy for river discharge, it is possible to estimate a reasonable curve for $\delta^{18}\text{O}_{\text{water}}$ values during the lifetime of the three analyzed oyster shells (Fig. 3D; Table S4; Figs. S19, S20). Following these considerations (see Supplementary Information 1 for further details), the reconstructed $\delta^{18}\text{O}_{\text{water}}$ values show more negative values in summer (when river discharge is highest) and more positive values during winter. Broadly, these $\delta^{18}\text{O}_{\text{water}}$ cycles also reflect seasonal salinity changes in agreement with present-day oceanographic studies (Fig. S1E)^{41,55}. Figure 3E shows the water temperatures calculated for the measured $\delta^{18}\text{O}_{\text{shell}}$ values and the estimated $\delta^{18}\text{O}_{\text{water}}$ values. Of course it needs to be highlighted that these calculated temperatures are already based on the proposed seasonal temperature extremes of 10 and 30 °C (Fig. S19). In summary, the first-order stable isotope cycles can be used to reconstruct seasonal changes in $\delta^{18}\text{O}_{\text{water}}$ cycles and therefore river discharge strength (reflecting precipitation). In contrast, the assumed seasonal water temperatures mainly rely on growth patterns in *C. gigas*, present-day observations, earlier literature information for the mid-Holocene, and the rough data from clumped isotope analyses.

Apart from first-order cycles, the $\delta^{18}\text{O}_{\text{shell}}$ and $\delta^{13}\text{C}_{\text{shell}}$ records show second-order excursions towards higher values within the broad minima (Fig. 3A, B). These excursions are too strong to be explained by simple variations in air temperature or river discharge, as there is no reason to propose strong cooling of surface waters by 5 to 7 °C in the study area or drastic decreases in river discharge during the summer months (compare discussion in Supplementary Information 1). Instead, the most likely explanation is regular summer upwelling in the study area, which leads to an influx of saline ocean water with higher $\delta^{18}\text{O}_{\text{water}}$ values. In addition, this upwelling might lead to higher $\delta^{13}\text{C}_{\text{water}}$ values and slightly lower water temperatures at the sea floor (possibly also indicated by the comparatively low summer temperature averages based on clumped isotopes; see above).

The second-order fluctuations in $\delta^{18}\text{O}_{\text{shell}}$ values can thus be used as a proxy for upwelling (Fig. 3F; Figs. S21, S22), but the second-order fluctuations in $\delta^{13}\text{C}_{\text{shell}}$ values might additionally record the influence of seasonal phytoplankton blooms and their subsequent decomposition⁴³. Such phytoplankton blooms during summer months have been recorded for the Yangtze River Delta in recent years and can be explained by the interplay of nutrient input from river discharge and influx of phosphates from upwelled water^{29,56,57}. In agreement with this interpretation, upwelling along the coasts of the East China Sea has been recorded in the last decades and also proposed for the Holocene (Supplementary Information 1)⁵⁸.

Comparisons with present-day conditions and future predictions

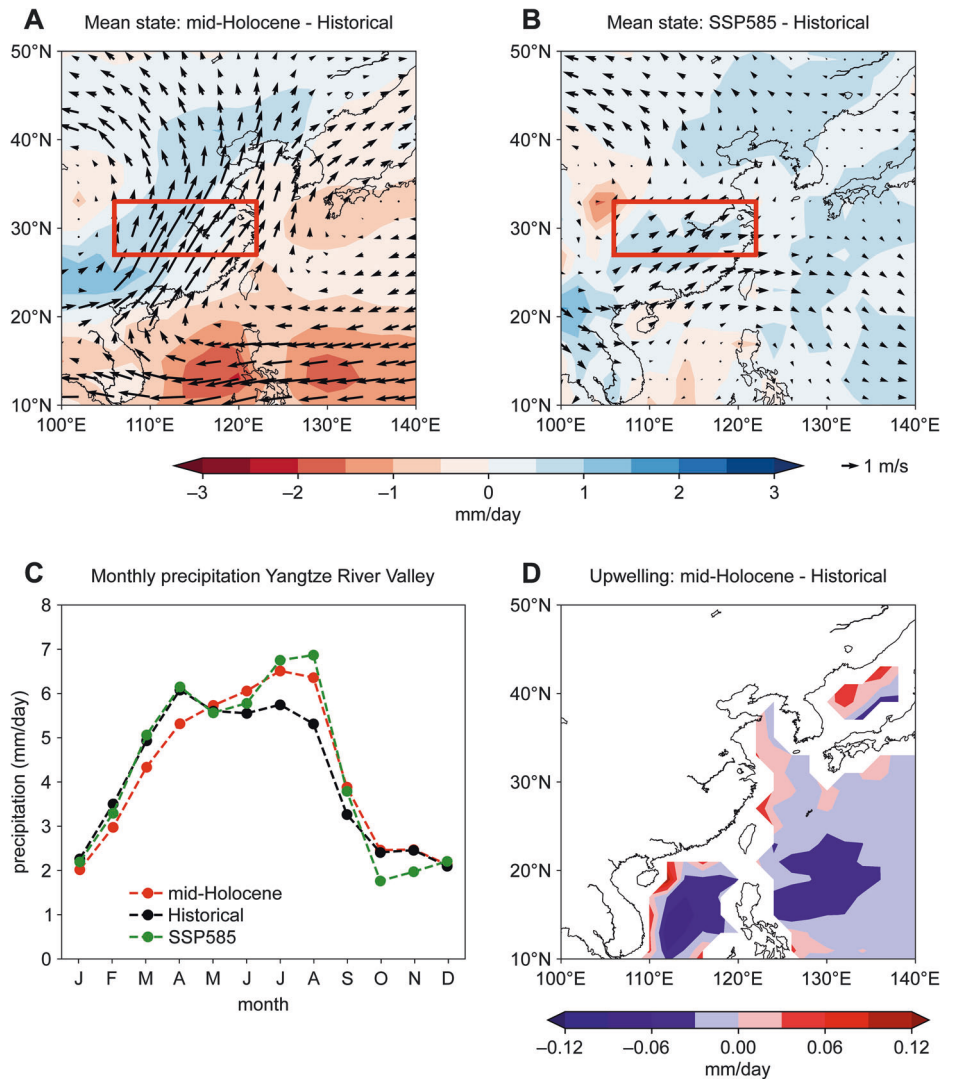
The stable isotope record of the analyzed shells generally shows a regular seasonal pattern, but for most cycles the decrease in $\delta^{13}\text{C}_{\text{shell}}$ values is delayed compared to the decrease in $\delta^{18}\text{O}_{\text{shell}}$ values (Fig. 3A, B; Figs. S7, S23–S25). This is particularly striking in shell 1, prominent in cycle 3 of shell 2, and less visible in shell 3. The presence of a delayed decrease in $\delta^{13}\text{C}_{\text{shell}}$ values can also be demonstrated when applying an internal age model (either based on constant growth rates or dated with the help of ShellChron⁵⁹; compare Supplementary Information 1). This indicates that while water temperatures are already rising in spring, river discharge still remains low for a considerable time. This is different to present-day conditions and points to a comparatively longer dry season extending into spring or early summer and increasing river discharge and rainfalls particularly during the summer months. Preliminary geochemical data of subrecent oyster shells from the coast of Jiangsu north of the Yangtze Delta show synchronous $\delta^{18}\text{O}_{\text{shell}}$ and $\delta^{13}\text{C}_{\text{shell}}$ cycles, which would be expected under present-day conditions (see Supplementary Information 1; Figs. S13, S14). A stronger seasonality in precipitation (and consequently river discharge) due to a larger impact of the summer monsoon has been proposed for warmer climate conditions such as the mid-Holocene interval and the future following on-going global warming^{60,61}. A stronger seasonality with more pronounced monsoonal rainfalls, river discharge, and wind strength can also explain a regular occurrence of summer upwelling (and phytoplankton blooms) in the mid-Holocene. Consequently, the presented data is in agreement with earlier proposals suggesting that the on-going and future global warming will cause stronger upwelling^{62,63} and stronger summer precipitation¹¹. In the Yangtze River Delta and the adjacent East China Sea, this might cause more common phytoplankton blooms and thereby more pronounced hypoxia. This finding has important repercussions for the region, impacting, for example, aquaculture or flood management. Ideally, further research on more Holocene oyster shells from East Asian coasts could elucidate regional patterns more clearly.

Comparisons with climate models' simulations

The geochemical results show prominent seasonal patterns in temperature, river discharge, and upwelling. The differences in the shape of the $\delta^{18}\text{O}_{\text{shell}}$ and $\delta^{13}\text{C}_{\text{shell}}$ curves can be interpreted to indicate a stronger seasonality in river discharge and precipitation with stronger monsoon rainfalls and/or drier winter months compared to today. This interpretation of the palaeo-proxy data can be used to test existing climate models and their reliability for reconstructing conditions in the mid-Holocene (and the future). The use of high-resolution archives such as bivalve shells has the additional advantage of enabling the reconstruction of seasonal environmental patterns.

The majority of used climate models predict drier conditions in the mid-Holocene compared to today⁶⁴, which does not agree with most climate reconstructions based on fossil data⁶⁵. Nine state-of-the-art climate models (Fig. 4A; Table S5) were used to simulate climate patterns for the Yangtze River Delta and adjacent East China Sea for the mid-Holocene (PMIP4), historical (CMIP6 DECK) and future time interval based on the SSP5-8.5 scenario (ScenarioMIP)^{66–68}. The SSP5-8.5 scenario was chosen, because it shows the most distinct differences to conditions today. Results from these climate models were examined separately as well as combined on a comparable 2° x 2° grid resolution (Figs. S26–S34). All used models simulate much stronger East Asian summer monsoon wind circulation during the

Fig. 4 | Results of climate models. The difference in the averaged boreal summer (June to August) precipitation and 850-hPa wind components between the mid-Holocene and historical simulations (A), and between the SSP5-8.5 and historical simulations (B) based on multi-model ensembles. The contour interval is 0.5 mm per day. The red rectangles are the Yangtze River Valley region. C Long-term mean monthly precipitation spatially averaged over the Yangtze River Valley region defined within the red rectangle of A and B. The red, black, and green dashed lines represent the mid-Holocene, the historical, and the SSP5-8.5 simulations, respectively. The model values are obtained from the multi-model ensemble using GISS-E2-1-G, IPSL-CM6A-LR, and NESM3. D The difference in the averaged boreal summer (June to August) upwelling between the mid-Holocene and historical simulations for the multi-model ensemble using GISS-E2-1-G, IPSL-CM6A-LR, and NESM3. The upwelling is computed by averaging the oceanic vertical velocity over the upper 100 m. The contour interval is 0.03 mm per day.



mid-Holocene compared to today (Fig. 4A, B)⁶⁹. All of them fail to simulate higher air temperatures for the mid-Holocene compared to today, thereby contradicting a large amount of fossil evidence and raising doubts on how well these models can predict future climate changes in the region^{4,9,64}. In more detail, the models vary considerably among themselves in the amount of precipitation simulated for the mid-Holocene in eastern China (Supplementary Information 1). A comparison between the model and palaeo-proxy data might help to determine, which of the climate models represent mid-Holocene rainfall patterns better and therefore might be better suited to predicting future changes in the region. In the present case, this comparison is qualitative with a seasonal resolution, because precise internal age models for the analyzed oysters are not available. Based on the data in the present study, three models (GISS-E2-1-G, IPSL-CM6A-LR, and NESM3) were found to be a good match by simulating less precipitation in winter and more rainfall during the summer compared to the historical period (Fig. 4C). Concerning future projections these models simulate monthly precipitation values similar to the historical period in the winter and spring seasons (December to May), but propose considerably more precipitation in the summer similar to the mid-Holocene simulation and the palaeo-proxy data (Fig. 4C). In addition, the same three models simulate stronger upwelling during the mid-Holocene in the East China Sea adjacent to the Yangtze River Delta, which also agrees well with the palaeo-proxy data (Fig. 4D). Consequently, it is suggested here that simulations based on these three climate models might be more realistic.

Conclusions

Stable isotope ($\delta^{18}\text{O}$, $\delta^{13}\text{C}$) data from three mid-Holocene oysters from the Yangtze River Delta in eastern China reflect prominent seasonal changes in temperature, precipitation, and river discharge. Results indicate regular summer upwelling in the study area and a longer dry season in winter compared to today. Because the mid-Holocene time interval was characterized by an up to 2 °C warmer climate in China compared to pre-industrial times, the results comprise a potential future scenario for the region considering on-going global warming. A comparison of available climate models shows that their simulations underestimate temperatures in East China during the mid-Holocene and that precipitation patterns vary considerably between climate models. All models simulate stronger monsoon winds in the mid-Holocene, which agrees with the regular presence of summer upwelling. Three models (GISS-E2-1-G, IPSL-CM6A-LR, and NESM3) were identified, which agree with the presented palaeo-proxy data in simulating more rainfalls in summer and less rainfalls in winter compared to today. Thus, the presented palaeo-proxy data can be used to control, correct, and improve existing climate models.

Methods

Geochemical analyses

The oyster shells used in the present study originate from collections of the Shanghai Natural History Museum and are now permanently stored in the collections of Nanjing University (School of Earth Sciences and

Engineering). They have a mid-Holocene age, were found in the central Yangtze River Delta (Fig. 1; 31°01'33.0" N, 121°03'13.0"E), and could be assigned to the genus *Crassostrea*. Today, this genus includes a series of similar species in East Asia with highly variable shell morphologies and sometimes not completely resolved taxonomic status^{42,49,70}. Some of the species described in literature produce identical shells and might be in fact invalid or can only be differentiated genetically^{71–76}. Despite these uncertainties, the collected fossil shells were assigned to *Crassostrea gigas* (Thunberg, 1793) based on general shell morphology and size⁴². This well-known species is the most common comparable oyster along the coasts of eastern Asia and has been used for stable isotope research previously^{30,43,77–79}. Based on macroscopic observations, three right valves were selected for this study (shells 1, 2, 3). The shells were cleaned and photographed externally (Fig. 2). Radiometric dating was conducted on extracted shell material for all three specimens at the Beta Analytic Testing Laboratory in Miami, USA.

Following external examinations, the shells were embedded in resin and cut through the hinge perpendicular to the growth lines (Fig. 2). Thin-sections were produced for the surfaces opposite the selected sampling areas. After examination with a petrographic microscope, the same sections were studied using a cold-cathodoluminescence microscope at the Nanjing Institute of Geology and Palaeontology, Chinese Academy of Sciences, China.

Sampling for stable isotope analyses was conducted using a computer-controlled micromill at the Nanjing Institute of Geology and Palaeontology, Chinese Academy of Sciences, China. Sampling tracks were placed parallel to the growth lines within the hinge at distances between 0.3 to 0.5 mm (Fig. 2). Stable isotope analyses were performed using a GasBench II IRMS system with a DELTA PLUS XP mass spectrometer at the School of Earth Sciences and Engineering, Nanjing University, China. Laboratory standards were analyzed at regular intervals to control the precision of the measured values. Based on the performance of standards, the analytical precision was better than $\pm 0.10\text{‰}$ (1 SD) for $\delta^{13}\text{C}$ and $\pm 0.18\text{‰}$ (1 SD) for $\delta^{18}\text{O}$ values. All measured values are reported in per mil relative to the Vienna Pee Dee belemnite (VPDB) scale using NBS-19.

The stable isotope data show strong cycles with sharp maxima and broad minima. Because $\delta^{18}\text{O}$ values of bivalve shells are negatively correlated to water temperature, the maxima are believed to indicate cold winter temperatures and the minima correspond to warm summer seasons. Following the identification of seasonal cycles in the stable isotope data, areas of the shells representing these summer and winter seasons were resampled for clumped isotope analyses at the Nanjing Institute of Geology and Palaeontology, Chinese Academy of Sciences, China. The acid hydrolysis, purification, and collection of the CO_2 gas were carried out in the automatic clumped isotope preparation instrument Isotope Batch Extraction System (IBEX 2). For each measurement, about 5 mg of the powder samples were weighed in a glass tube and placed in an autosampler dropping into a common acid bath. In this bath, the powder was fully reacted with phosphoric acid with a density of 1.92 g/cm^3 at constant temperatures of 90°C . The produced CO_2 was then carried by a helium flow current through a liquid nitrogen cold trap and GC trap for purification. The purified CO_2 was imported into a ThermoFisher Scientific 253 Plus Mass spectrometer for clumped isotopes measurement. This mass spectrometer is equipped with six Faraday cups measuring m/z 44–49 and an additional 47.5 cup for monitoring background baselines. Peak scans were performed for several days for the pressure baseline correction⁸⁰. Clumped isotope results are reported relative to I-CDES through an empirical transfer function (ETF) based on measurements of ETH standards and their given I-CDES values (ETH-1 = 0.2052‰ ; ETH-2 = 0.2085‰ ; ETH-3 = 0.6132‰ ; ETH-4 = 0.4505‰)⁸¹. In addition, the carbonate standard IAEA603 (i.e. IAEA-C1) was analyzed together with the samples to monitor long-term accuracy and reproducibility of Δ_{47} values. Multiple analyses yielded an average value of 0.3113‰ ($n = 16$; $\text{SD} = 0.038$), which is indistinguishable from the accepted value for IAEA-C1 of $0.3018 \pm 0.0025\text{‰}$ (95% CL)⁸¹. Isotopic values were calculated using the latest International Union of Pure and Applied Chemistry values^{82,83}. AFF was needless following the I-CDES standardization since the carbonate standards used for the ETF undergo the

same acid reaction as the samples⁸¹. All corrections and calibrations were conducted using the Easotope software package⁸⁴. The mineral growth temperatures are calculated following the equation of Meinicke et al.^{46,47} and alternative temperatures based on Anderson et al.⁸⁵ are presented as well in the Supplementary Information 1 and Supplementary Data 2.

Climate models

The numerical simulations datasets are from models' outputs provided by the CMIP6 World Climate Research Programme's Working Group on Coupled Modeling (Eyring et al., 2016). The simulations used are the mid-Holocene experiment (PMIP4), the historical experiment (CMIP DECK), and the SSP5-8.5 future scenario projection (ScenarioMIP)^{67,68}. The first 100 years of the mid-Holocene simulations, the first 100 years of the historical simulations (1850–1949), and the last 50 years of the SSP5-8.5 simulations (2051–2100) were used in the analyses. The SSP5-8.5 future scenario was not available for GISS-E2-1-G. With the exception of GISS-E2-1-G, in which the ensemble member is r1i1p1f2, for all the remaining models the ensemble member r1i1p1f1 is used. Table S5 in Supplementary Information 1 shows the details of the nine climate models used in this study. In the analyses, all models are interpolated to a common $2^\circ \times 2^\circ$ grid resolution. The main differences between the mid-Holocene simulation and the historical and SSP5-8.5 simulations are related to the parametrizations of the Earth's eccentricity, obliquity, and precession. The mid-Holocene simulation set the eccentricity, obliquity, and precession to 0.018682 , 24.105° , and 0.87° , respectively, whilst the historical and SSP5-8.5 simulations are set to 0.016764 , 23.459° , and 100.33° , respectively⁸⁶. The atmospheric CO_2 concentration is also different, with 264.4 ppmv for the mid-Holocene period, $\sim 400\text{ ppmv}$ in 2014 for historical simulation, and $\sim 1100\text{ ppmv}$ in 2100 for the SSP5-8.5 future scenario. Notice that for historical and SSP5-8.5 simulations the CO_2 concentration increases throughout the experiments.

Data availability

All data of this study together with additional results and discussions are given in the extensive Supplementary Information 1 and Supplementary Data 1 and 2.

Received: 14 November 2023; Accepted: 30 August 2024;

Published online: 08 September 2024

References

- An, Z. et al. Asynchronous Holocene optimum of the East Asian monsoon. *Quat. Sci. Rev.* **19**, 743–762 (2000).
- Dykoski, C. A. et al. A high-resolution, absolute-dated Holocene and deglacial Asian monsoon record from Dongge Cave, China. *Earth Planet. Sci. Lett.* **233**, 71–86 (2005).
- Zhou, X. et al. Time-transgressive onset of the Holocene Optimum in the East Asian monsoon region. *Earth Planet. Sci. Lett.* **456**, 39–46 (2016).
- Dong, Y. et al. The Holocene temperature conundrum answered by mollusk records from East Asia. *Nat. Commun.* **13**, 5133 (2022).
- Chen, Z., Wang, Z., Schneiderman, J., Tao, J. & Cai, Y. Holocene climate fluctuations in the Yangtze delta of eastern China and the Neolithic response. *Holocene* **15**, 915–924 (2005).
- Wang, Z. et al. Early mid-Holocene sea-level change and coastal environmental response on the southern Yangtze delta plain, China: implications for the rise of Neolithic culture. *Quat. Sci. Rev.* **35**, 51–62 (2012).
- Zheng, Y., Sun, G. & Chen, X. Response of rice cultivation to fluctuating sea level during the Mid-Holocene. *Chin. Sci. Bull.* **57**, 370–378 (2012).
- Liu, Y. et al. Middle Holocene coastal environment and the rise of the Liangzhu City complex on the Yangtze Delta, China. *Quat. Res.* **84**, 326–334 (2015).
- Li, J. et al. Quantitative Holocene climatic reconstructions for the lower Yangtze region of China. *Clim. Dyn.* **50**, 1101–1113 (2018).

10. Lv, Y., Li, W., Wen, J., Xu, H. & Du, S. Population pattern and exposure under sea level rise: Low elevation coastal zone in the Yangtze River Delta, 1990–2100. *Clim. Risk Manag.* **33**, 100348 (2021).
11. IPCC. Climate Change 2023: Synthesis Report. Contribution of Working Groups I, II and III to the Sixth Assessment Report on the Intergovernmental Panel on Climate Change. IPCC, Geneva, Switzerland, 184 pp. (2023).
12. Qiao, F. et al. Coastal upwelling in the East China Sea in winter. *J. Geophys. Res.* **111**, S11S06 (2006).
13. Hu, M. & Zhao, C. Upwelling in Zhejiang coastal areas during summer detected by satellite observations. *J. Remote Sens.* **12**, 297–304 (2008).
14. Kim, S.-B. et al. Sea surface salinity variability in the East China Sea observed by the Aquarius instrument. *J. Geophys. Res.: Oceans* **119**, 7016–7028 (2014).
15. Yang, S. L., Xu, K. H., Milliman, J. D., Yang, H. F. & Wu, C. S. Decline of Yangtze River water and sediment discharge: impact from natural and anthropogenic changes. *Sci. Rep.* **5**, 12581 (2015).
16. Hu, J. & Wang, X. H. Progress on upwelling studies in the China seas. *Rev. Geophys.* **54**, 653–673 (2016).
17. Yu, X., Zhang, W. & Houtink, A. J. F. Impact of river discharge seasonality change on tidal duration asymmetry in the Yangtze River Estuary. *Sci. Rep.* **10**, 6304 (2020).
18. Delcroix, T. & Murtugudde, R. Sea surface salinity changes in the East China Sea during 1997–2001: Influence of the Yangtze River. *J. Geophys. Res.* **107**, 8008 (2002).
19. Chen, Z., Li, J., Shen, H. & Wang, Z. Yangtze River of China: Historical analysis of discharge variability and sediment flux. *Geomorphology* **41**, 77–91 (2001).
20. Chen, X., Wang, X. & Guo, J. Seasonal variability of the sea surface salinity in the East China Sea during 1990–2002. *J. Geophys. Res.* **111**, C05008 (2006).
21. Sun, T., Yang, Z. F., Shen, Z. F. & Zhao, R. Environmental flows for the Yangtze Estuary based on salinity objectives. *Commun. Nonlinear Sci. Numer. Simul.* **14**, 959–971 (2009).
22. Son, S., Yoo, S. & Noh, J.-H. Spring phytoplankton bloom in the fronts of the East China Sea. *Ocean Sci. J.* **41**, 181–189 (2006).
23. Chen, C.-C., Gong, G.-C. & Shiah, F.-K. Hypoxia in the East China Sea: one of the largest coastal low-oxygen areas in the world. *Mar. Environ. Res.* **64**, 399–408 (2007).
24. Chen, J. et al. Relationships between long-term trend of satellite-derived chlorophyll-*a* and hypoxia off the Changjiang Estuary. *Estuaries Coasts* **40**, 1055–1065 (2017).
25. Chen, C.-C., Shiah, F.-K., Gong, G.-C. & Chen, T.-Y. Impact of upwelling on phytoplankton blooms and hypoxia along the Chinese coast in the East China Sea. *Mar. Pollut. Bull.* **167**, 112288 (2021).
26. Chen, Y., Shi, H. & Zhao, H. Summer phytoplankton blooms induced by upwelling in the western South China Sea. *Front. Mar. Sci.* **8**, 740130 (2021).
27. Pei, S., Shen, Z., Laws, E. A. Nutrient dynamics of the upwelling area in the Changjiang Estuary. In *Studies of the biogeochemistry of typical estuaries and bays in China* (ed. Shen, Z.). Springer Earth System Sciences, 105–124 (2009).
28. Li, X. et al. Historical trends of hypoxia in Changjiang River estuary: Applications of chemical biomarkers and microfossils. *J. Mar. Syst.* **86**, 57–68 (2011).
29. Wang, Y. et al. Phytoplankton blooms off a high turbidity estuary: a case study in the Changjiang River Estuary. *J. Geophys. Res.: Oceans* **124**, 8036–8059 (2019).
30. Fan, C., Koeniger, P., Wang, H. & Frechen, M. Ligamental increments of the mid-Holocene Pacific oyster *Crassostrea gigas* are reliable independent proxies for seasonality in the western Bohai Sea, China. *Palaeogeogr. Palaeoclimatol. Palaeoecol.* **299**, 437–448 (2011).
31. Wierzbowski, H. Detailed oxygen and carbon isotope stratigraphy of the Oxfordian in Central Poland. *Int. J. Earth Sci.* **91**, 304–314 (2002).
32. Williams, M. et al. Sea ice extent and seasonality for the Early Pliocene northern Weddell Sea. *Palaeogeogr. Palaeoclimatol. Palaeoecol.* **292**, 306–318 (2010).
33. Alberti, M., Fürsich, F. T. & Pandey, D. K. Seasonality in low latitudes during the Oxfordian (Late Jurassic) reconstructed via high-resolution stable isotope analysis of the oyster *Actinostreon marshi* (J. Sowerby, 1814) from the Kachchh Basin, western India. *Int. J. Earth Sci.* **102**, 1321–1336 (2013).
34. Langlet, D. et al. Experimental and natural cathodoluminescence in the shell of *Crassostrea gigas* from Thau lagoon (France): ecological and environmental implications. *Mar. Ecol. Prog. Ser.* **317**, 143–156 (2006).
35. Lartaud, F. et al. Mn labelling of living oysters: Artificial and natural cathodoluminescence analyses as a tool for age and growth rate determination of *C. gigas* (Thunberg, 1793) shells. *Aquaculture* **300**, 206–217 (2010).
36. Barbin, V. Application of cathodoluminescence microscopy to recent and past biological materials: a decade of progress. *Mineral. Petrol.* **107**, 353–362 (2013).
37. Judd, E. J., Wilkinson, B. H. & Ivany, L. C. The life and time of clams: Derivation of intra-annual growth rates from high-resolution oxygen isotope profiles. *Palaeogeogr. Palaeoclimatol. Palaeoecol.* **490**, 70–83 (2018).
38. Urey, H. C., Lowenstam, H. A., Epstein, S. & McKinney, C. R. Measurement of paleotemperatures and temperatures of the Upper Cretaceous of England, Denmark, and the southeastern United States. *Bull. Geol. Soc. Am.* **62**, 399–416 (1951).
39. Epstein, S., Buchsbaum, R., Lowenstam, H. & Urey, H. C. Carbonate-water isotopic temperature scale. *Bull. Geol. Soc. Am.* **62**, 417–426 (1951).
40. Anderson, T. F. & Arthur, M. A. Stable isotopes of oxygen and carbon and their application to sedimentological and paleoenvironmental problems. *SEPM Short. Course* **10**, 1–151 (1983).
41. Ye, F., Deng, W., Xie, L., Wei, G. & Jia, G. Surface water $\delta^{18}\text{O}$ in the marginal China seas and its hydrological implications. *Estuar. Coast. Shelf Sci.* **147**, 25–31 (2014).
42. Quayle, D. B. Pacific oyster culture in British Columbia. *Can. Bull. Fish. Aquat. Sci.* **218**, 241 p. (1988).
43. Wang, H., Keppens, E. & Nielsen, P. & van Riet, A. Oxygen and carbon isotope study of the Holocene oyster reefs and paleoenvironmental reconstruction on the northwest coast of Bohai Bay, China. *Mar. Geol.* **124**, 289–302 (1995).
44. Kirby, M. X., Soniat, T. M. & Spero, H. J. Stable isotope sclerochronology of Pleistocene and Recent oyster shells (*Crassostrea virginica*). *Palaaios* **13**, 560–569 (1998).
45. Lartaud, F. et al. A latitudinal gradient of seasonal temperature variation recorded in oyster shells from the coastal waters of France and the Netherlands. *Facies* **56**, 13–25 (2010).
46. Meinicke, N. et al. A robust calibration of the clumped isotopes to temperature relationship for foraminifers. *Geochim. Cosmochim. Acta* **270**, 160–183 (2020).
47. de Winter, N. J. et al. Temperature dependence of clumped isotopes (Δ_{47}) in aragonite. *Geophys. Res. Lett.* **49**, e2022GL099479 (2022).
48. Bougrier, S., Geairon, P., Deslous-Paoli, J. M., Bacher, C. & Jonquères, G. Allometric relationships and effects of temperature on clearance and oxygen consumption rates of *Crassostrea gigas* (Thunberg). *Aquaculture* **134**, 143–154 (1995).
49. Nehring, S. NOBANIS – Invasive alien species fact sheet – *Crassostrea gigas*. – Online Database of the European Network on Invasive Alien Species, NOBANIS. www.nobanis.org, date of access: 2022/09/30 (2011).

50. Berger, W. H. & Vincent, E. Deep-sea carbonates: reading the carbon-isotope signal. *Geol. Rundsch.* **75**, 249–269 (1986).
51. Grossman, E. L. & Ku, T.-L. Oxygen and carbon isotope fractionation in biogenic aragonite: temperature effects. *Chem. Geol.: Isot. Geosci. Sect.* **59**, 59–74 (1986).
52. Lorrain, A. et al. $\delta^{13}\text{C}$ variation in scallop shells: increasing metabolic carbon contribution with body size? *Geochim. Cosmochim. Acta* **68**, 3509–3519 (2004).
53. McConnaughey, T. A. & Gillikin, D. P. Carbon isotopes in mollusk shell carbonates. *Geo-Mar. Lett.* **28**, 287–299 (2008).
54. Surge, D., Lohmann, K. C. & Dettman, D. L. Controls on isotopic chemistry of the American oyster, *Crassostrea virginica*: implications for growth patterns. *Palaeogeogr. Palaeoclimatol. Palaeoecol.* **172**, 283–296 (2001).
55. Zhang, J., Letolle, R., Martin, J. M., Jusserand, C. & Mouchel, J. M. Stable oxygen isotope distribution in the Huanghe (Yellow River) and the Changjiang (Yangtze River) estuarine systems. *Continental Shelf Res.* **10**, 369–384 (1990).
56. Yamaguchi, H. et al. Seasonal and summer interannual variations of SeaWiFS chlorophyll α in the Yellow Sea and East China Sea. *Prog. Oceanogr.* **105**, 22–29 (2012).
57. Yang, D., Yin, B., Sun, J. & Zhang, Y. Numerical study on the origins and the forcing mechanism of the phosphate in upwelling areas off the coast of Zhejiang province, China in summer. *J. Mar. Syst.* **123–124**, 1–18 (2013).
58. Xu, T. et al. Holocene sedimentary evolution and hypoxia development in the subaqueous Yangtze (Changjiang) Delta, China. *Mar. Geol.* **430**, 106359 (2020).
59. de Winter, N. J. ShellChron 0.4.0: a new tool for constructing chronologies in accretionary carbonate archives from stable oxygen isotope profiles. *Geosci. Model Dev.* **15**, 1247–1267 (2022).
60. Wang, Y. et al. The Holocene Asian monsoon: links to solar changes and North Atlantic climate. *Science* **308**, 854–857 (2005).
61. Katzenberger, A., Schewe, J., Pongratz, J. & Levermann, A. Robust increase of Indian monsoon rainfall and its variability under future warming in CMIP6 models. *Earth Syst. Dyn.* **12**, 367–386 (2021).
62. Bakun, A. Global climate change and intensification of coastal ocean upwelling. *Science* **247**, 198–201 (1990).
63. McGregor, H. V., Dima, M., Fischer, H. W. & Mulitza, S. Rapid 20th-century increase in coastal upwelling off Northwest Africa. *Science* **315**, 637–639 (2007).
64. Wu, Y., Liu, Y., Zhou, W. & Zhang, J. The mid-Holocene East Asian summer monsoon simulated by PMIP4-CMIP6 and PMIP3-CMIP5: Model uncertainty and its possible sources. *Glob. Planet. Change* **219**, 103986 (2022).
65. Chen, W. et al. Mid-Holocene high-resolution temperature and precipitation gridded reconstructions over China: Implications for elevation-dependent temperature changes. *Earth Planet. Sci. Lett.* **593**, 117656 (2022).
66. Eyring, V. et al. Overview of the Coupled Model Intercomparison Project Phase 6 (CMIP6) experimental design and organization. *Geosci. Model Dev.* **9**, 1937–1958 (2016).
67. O'Neill, B. C. et al. The Scenario Model Intercomparison Project (ScenarioMIP) for CMIP6. *Geosci. Model Dev.* **9**, 3461–3482 (2016).
68. Kageyama, M. et al. The PMIP4 contribution to CMIP6 - Part 1: Overview and over-arching analysis plan. *Geosci. Model Dev.* **11**, 1033–1057 (2018).
69. Jiang, D., Lang, X., Tian, Z. & Ju, L. Mid-Holocene East Asian summer monsoon strengthening: insights from Paleoclimate Modeling Intercomparison Project (PMIP) simulations. *Palaeogeogr. Palaeoclimatol. Palaeoecol.* **369**, 422–429 (2013).
70. Guo, X., Ford, S. E. & Zhang, F. Molluscan aquaculture in China. *J. Shellfish Res.* **18**, 19–31 (1999).
71. Huvet, A. et al. Is fertility of hybrids enough to conclude that the two oysters *Crassostrea gigas* and *Crassostrea angulata* are the same species? *Aquat. Living Resour.* **15**, 45–52 (2002).
72. Soletchnik, P. et al. A comparative field study of growth, survival and reproduction of *Crassostrea gigas*, *C. angulata* and their hybrids. *Aquat. Living Resour.* **15**, 243–250 (2002).
73. Boudry, P., Heurtebise, S. & Lapègue, S. Mitochondrial and nuclear DNA sequence variation of presumed *Crassostrea gigas* and *Crassostrea angulata* specimens: a new oyster species in Hong Kong? *Aquaculture* **228**, 15–25 (2003).
74. Xia, J., Yu, Z. & Kong, X. Identification of seven *Crassostrea* oysters from the South China Sea using PCR-RFLP analysis. *J. Mollusca. Stud.* **75**, 139–146 (2009).
75. Xia, J., Wu, X., Xiao, S. & Yu, Z. Mitochondrial DNA and morphological identification of a new cupped oyster species *Crassostrea dianbaiensis* (Bivalvia: Ostreidae) in the South China Sea. *Aquat. Living Resour.* **27**, 41–48 (2014).
76. Wang, J., Xu, F., Li, L. & Zhang, G. A new identification method for five species of oysters in genus *Crassostrea* from China based on high-resolution melting analysis. *Chin. J. Oceanol. Limnol.* **32**, 419–425 (2014).
77. Ullmann, C. V., Wiechert, U. & Korte, C. Oxygen isotope fluctuations in a modern North Sea oyster (*Crassostrea gigas*) compared with annual variations in seawater temperature: implications for palaeoclimate studies. *Chem. Geol.* **277**, 160–166 (2010).
78. Ullmann, C. V., Böhm, F., Rickaby, R. E. M., Wiechert, U. & Korte, C. The Giant Pacific Oyster (*Crassostrea gigas*) as a modern analog for fossil ostreoids: isotopic (Ca, O, C) and elemental (Mg/Ca, Sr/Ca, Mn/Ca) proxies. *Geochem. Geophys. Geosyst.* **14**, 4109–4120 (2013).
79. de Winter, N. J. et al. Multi-isotopic and trace element evidence against different formation pathways for oyster microstructures. *Geochim. Cosmochim. Acta* **308**, 326–352 (2021).
80. Bernasconi, S. M. et al. Background effects on Faraday collectors in gas-source mass spectrometry and implications for clumped isotope measurements. *Rapid Commun. Mass Spectrom.* **27**, 603–612 (2013).
81. Bernasconi, S. M. et al. InterCarb: A community effort to improve interlaboratory standardization of the carbonate-clumped isotope thermometer using carbonate standards. *Geochem., Geophys. Geosyst.* **22**, e2020GC009588 (2021).
82. Brand, W. A., Assonov, S. S. & Coplen, T. B. Correction for the ^{17}O interference in $\delta(^{13}\text{C})$ measurements when analyzing CO_2 with stable isotope mass spectrometry (IUPAC technical report). *Pure Appl. Chem.* **82**, 1719–1733 (2010).
83. Daëron, M., Blamart, D., Peral, M. & Affek, H. P. Absolute isotopic abundance ratios and the accuracy of Δ_{47} measurements. *Chem. Geol.* **442**, 83–96 (2016).
84. John, C. M. & Bowen, D. Community software for challenging isotope analysis: first applications of 'Easotope' to clumped isotopes. *Rapid Commun. Mass Spectrom.* **30**, 2285–2300 (2016).
85. Anderson, N. T. et al. A unified clumped isotope thermometer calibration (0.5–1100 °C) using carbonate-based standardization. *Geophys. Res. Lett.* **48**, e2020GL092069 (2021).
86. Otto-Bliesner, B. L. et al. The PMIP4 contribution to CMIP6 - Part 2: Two interglacials, scientific objective and experimental design for Holocene and Last Interglacial simulations. *Geosci. Model Dev.* **10**, 3979–4003 (2017).
87. Zhu, C. et al. On the Holocene sea-level highstand along the Yangtze Delta and Ningshao Plain, East China. *Chin. Sci. Bull.* **48**, 2672–2683 (2003).
88. Zhang, Q. et al. Paleo-environmental changes in the Yangtze Delta during past 8000 years. *J. Geogr. Sci.* **14**, 105–112 (2004).
89. Innes, J. B., Zong, Y., Wang, Z. & Chen, Z. Climatic and palaeoecological changes during the mid- to Late Holocene transition in eastern China: high-resolution pollen and non-pollen palynomorph analysis at Pingwang, Yangtze coastal lowlands. *Quat. Sci. Rev.* **99**, 164–175 (2014).

Acknowledgements

MA gratefully acknowledges financial support from the State Key Laboratory of Palaeobiology and Stratigraphy of the Nanjing Institute of Geology and Palaeontology, Chinese Academy of Sciences (No. 223101). Furthermore, the research was supported by the Strategic Priority Research Program of the Chinese Academy of Sciences (Grant no. XDB26000000), the National Natural Science Foundation of China (Grant no. 41922011), and the Fundamental Research Funds for the Central Universities (No. 0206-14380219). SFV is supported by the National Natural Science Foundation of China (Grant no. 42050410322) and the GeoX Interdisciplinary Research Funds for the Frontiers Science Center for Critical Earth Material Cycling, Nanjing University (Grant no. 020714380200). Takaaki Konabe Watanabe (Kiel, Germany) helped with statistical analyses. We thank Niels de Winter, Weizhe Chen, the anonymous reviewer, and the editors for their constructive comments during the peer-review process.

Author contributions

M.A. contributed to the conceptualization, design, methodology, sample preparation and collection, laboratory work, data analysis, original draft, and revision of the manuscript. S.F.V. contributed to the design, methodology, data analysis, original draft, and revision of the manuscript. B.C. contributed to the design, methodology, laboratory work, data analysis, original draft, and revision of the manuscript. L.H. contributed to the sample preparation and collection, laboratory work, and data analysis. Z.F. contributed to the sample preparation and collection, laboratory work, and data analysis. B.Z. contributed to the conceptualization, design, sample preparation, and collection. Y.P. contributed to the conceptualization, design, methodology, sample preparation and collection, data analysis, original draft, and revision of the manuscript.

Funding

Open Access funding enabled and organized by Projekt DEAL.

Competing interests

The authors declare no competing interests.

Additional information

Supplementary information The online version contains supplementary material available at <https://doi.org/10.1038/s43247-024-01668-1>.

Correspondence and requests for materials should be addressed to Matthias Alberti or Yanhong Pan.

Peer review information *Communications Earth & Environment* thanks Niels de Winter, Weizhe Chen and the other, anonymous, reviewer(s) for their contribution to the peer review of this work. Primary Handling Editors: Sze Ling Ho, Aliénor Laverne, and Carolina Ortiz Guerrero. A peer review file is available

Reprints and permissions information is available at <http://www.nature.com/reprints>

Publisher's note Springer Nature remains neutral with regard to jurisdictional claims in published maps and institutional affiliations.

Open Access This article is licensed under a Creative Commons Attribution 4.0 International License, which permits use, sharing, adaptation, distribution and reproduction in any medium or format, as long as you give appropriate credit to the original author(s) and the source, provide a link to the Creative Commons licence, and indicate if changes were made. The images or other third party material in this article are included in the article's Creative Commons licence, unless indicated otherwise in a credit line to the material. If material is not included in the article's Creative Commons licence and your intended use is not permitted by statutory regulation or exceeds the permitted use, you will need to obtain permission directly from the copyright holder. To view a copy of this licence, visit <http://creativecommons.org/licenses/by/4.0/>.

© The Author(s) 2024